A physics-based shock capturing method for unsteady laminar and turbulent flows

P. Fernandez[*], N.C. Nguyen[†], J. Peraire [‡]

Massachusetts Institute of Technology, Cambridge, MA 02139, United States

We present a shock capturing method for unsteady laminar and turbulent flows. The proposed approach relies on physical principles to increase selected transport coefficients and resolve unstable sharp features, such as shock waves and strong thermal and shear gradients, over the smallest distance allowed by the discretization. In particular, we devise various sensors to detect when the shear viscosity, bulk viscosity and thermal conductivity of the fluid do not suffice to stabilize the numerical solution. In such cases, the transport coefficients are increased as necessary to optimally resolve these features with the available resolution. The performance of the method is illustrated through numerical simulation of external and internal flows in transonic, supersonic, and hypersonic regimes.

I. Introduction

Insufficient resolution to capture sharp features in a fluid flow may lead to numerical oscillations and nonlinear instability. In the case of transonic, supersonic and hypersonic flows, a number of such under-resolved sharp features may appear and lead to inaccurate results and even the simulation breakdown, including shock waves, strong thermal gradients and thin shear layers. Despite the large number of works on shock capturing since the dawn of computational fluid dynamics, numerical simuation of unsteady flows involving shocks remains a challenging problem,[18,27,39] particularly for high-order methods.[17] First, many shock capturing methods have been developed for steady-state or inviscid problems, but their extension to unsteady and viscous flows is not straightforward. Second, the majority of the existing methods are by construction not able to stabilize sharp features other than shock waves. This compromises robustness and limits the applicability to some particular types of flows. In order to enable simulation of transonic, supersonic and hypersonic unsteady flows, a method to detect and stabilize all sources of instability is required. While this will be referred to as a *shock capturing* method for consistency with the common terminology in the literature, we emphasize the need to deal with other numerical instabilities arising in the simulation of unsteady flows. We shall refer to them as *unstable subgrid-scale (SGS)* features.

Prior to describing the shock capturing method, we present an overview of approaches in the literature for the detection and stabilization of shock waves and other unstable SGS features. As for shock detection, perhaps the most popular approach is to take advantage of the strong compression that a fluid undergoes accross a shock wave and use the divergence of the velocity field as a shock sensor.[3,28,29] An assessment of dilatation-based shock detection methods is presented in.[41] In our experience, the existing methods in this category provide non-oscillatory, well-resolved shocks for steady flows, such as laminar and Reynolds-averaged turbulent flows, but they fail to perform well in unsteady flows. Alternatively, a number of methods rely on the non-smoothness of the numerical solution to detect shocks and other unstable features.[9,19–22,32,35,36] Among them, the sensor by Krivodonova et al.[22] takes advantage of the expected convergence rate of discontinuous Galerkin (DG) methods in smooth regions to detect shocks. By construction, this sensor is limited to fairly high-order DG methods, hyperbolic systems of conservation laws such as the Euler equations, and stabilization mechanisms that do not introduce artificial viscosity. The shock sensor by Persson[35,36] is based on the decay rate of the coefficients of the DG polynomial approximation. Like the sensor by Krivodonova et al., it requires accuracy orders beyond ~ 5 to provide acceptable results. Other approaches that rely on high-order derivatives of the numerical solution include.[9,19,20,32] Again, these methods only apply to schemes for which such derivatives can be accurately computed, such as spectral-type DG methods and high-order finite difference methods on structured meshes and simple geometries. Also, most methods based on the smoothness of the numerical solution involve user-defined

---

[*]PhD Student, Department of Aeronautics and Astronautics, MIT. Email: pablof@mit.edu. AIAA Student Member.

[†]Principal Research Scientist, Department of Aeronautics and Astronautics, MIT. Email: cuongng@mit.edu. AIAA Member.

[‡]H.N. Slater Professor and Department Head of Aeronautics and Astronautics, MIT. Email: peraire@mit.edu. AIAA Fellow.

parameters that are flow-dependent and usually hard to tune for new problems. This compromises the adoption of these methods in industry due to the high robustness and flexibility that these applications require.

Regarding stabilization, most methods lie within one of the following two categories: Limiters and artificial viscosity. Limiters, in the form of flux limiters[4,5,23] or solution limiters,[6,22,24,25,37,40,42] are not well suited for implicit time integration schemes, and also pose challenges for high-order methods on complex geometries. As for artificial viscosity methods, Laplacian-based[15,26,28,29,35,36] and physics-based[1,9,19,20,32,35,38] approaches have been proposed. An assessment of artificial viscosity methods for unsteady flows is presented in.[27] In general, these methods perform poorly for unsteady flows and/or require accurate high-order derivatives of the numerical solution.

In this paper, we present a shock capturing method for unsteady laminar and turbulent flows that aims to address the limitations above. To that end, we first introduce a series of sensors to detect different types of unstable SGS features, and then present an artificial viscosity procedure to stabilize them with the available resolution. In particular, the remainder of the paper is structured as follows. In Section II, we present the numerical methods used to discretize the Navier-Stokes equations. Sections III and IV describe the sensors and the procedure to stabilize the numerical scheme, respectively. Section V illustrates the performance of the method for external and internal flows in transonic, supersonic, and hypersonic regimes. We conclude the paper with some remarks and future work in Section VI.

II.   Flow discretization

A.   Governing equations

We consider the unsteady, compressible Navier-Stokes equations written in conservation form as

$$
\begin{aligned}
\boldsymbol{q} - \nabla \boldsymbol{u} &= 0, \quad \text{in } \Omega \times (0, T), \\
\frac{\partial \boldsymbol{u}}{\partial t} + \nabla \cdot \boldsymbol{F}(\boldsymbol{u}, \boldsymbol{q}) &= 0, \quad \text{in } \Omega \times (0, T),
\end{aligned}
\tag{1}
$$

where $T > 0$, $\Omega \subset \mathbb{R}^d$ is a bounded open physical domain with piecewise smooth boundary $\partial \Omega$, $\boldsymbol{u} = (\rho, \rho v_j, \rho E)$, $j = 1, ..., d$ is the m-dimensional vector of conserved quantities, and $\boldsymbol{F}(\boldsymbol{u}, \boldsymbol{q})$ are the Navier-Stokes fluxes of dimension $m \times d$,

$$
\boldsymbol{F}(\boldsymbol{u}, \boldsymbol{q}) = \begin{pmatrix} \rho v_j \\ \rho v_i v_j + \delta_{ij} p \\ v_j (\rho E + p) \end{pmatrix} - \begin{pmatrix} 0 \\ \tau_{ij} \\ v_i \tau_{ij} + f_j \end{pmatrix}.
\tag{2}
$$

For a Newtonian, calorically perfect gas in thermodynamic equilibrium, the viscous stress tensor, heat flux, and pressure are given by

$$
\tau_{ij} = \mu \left[\left(\frac{\partial v_i}{\partial x_j} + \frac{\partial v_j}{\partial x_i} \right) - \frac{2}{3} \frac{\partial v_k}{\partial x_k} \delta_{ij} \right] + \beta \frac{\partial v_k}{\partial x_k} \delta_{ij}, \quad f_j = -\frac{c_p \mu}{Pr} \frac{\partial T}{\partial x_j}, \quad p = (\gamma - 1) \rho \left(E - \frac{1}{2} v_k v_k \right),
\tag{3}
$$

respectively, where μ denotes the dynamic (shear) viscosity, β the bulk viscosity, c_p is the specific heat at constant pressure, Pr the Prandtl number, and γ the ratio of specific heats. In particular, $Pr = 0.71$, $\gamma = 1.4$ and $\beta = 0$ for air.

B.   Numerical discretization

We consider hybridized discontinuous Galerkin (DG) methods,[13] which generalize the HDG[7,30,33] and the EDG[7,8,34] methods, for the numerical simulation of unsteady flows. The hybridized DG discretization of the compressible Navier-Stokes equations reads as follows: Find $\left(\boldsymbol{q}_h(t), \boldsymbol{u}_h(t), \widehat{\boldsymbol{u}}_h(t) \right) \in \mathcal{Q}_h^k \times \mathcal{V}_h^k \times \mathcal{M}_h^k$ such that

$$
\left(\boldsymbol{q}_h, \boldsymbol{r} \right)_{\mathcal{T}_h} + \left(\boldsymbol{u}_h, \nabla \cdot \boldsymbol{r} \right)_{\mathcal{T}_h} - \left\langle \widehat{\boldsymbol{u}}_h, \boldsymbol{r} \cdot \boldsymbol{n} \right\rangle_{\partial \mathcal{T}_h} = 0,
\tag{4a}
$$

$$
\left(\frac{\partial \boldsymbol{u}_h}{\partial t}, \boldsymbol{w} \right)_{\mathcal{T}_h} - \left(\boldsymbol{F}(\boldsymbol{u}_h, \boldsymbol{q}_h), \nabla \boldsymbol{w} \right)_{\mathcal{T}_h} + \left\langle \widehat{\boldsymbol{f}}_h(\widehat{\boldsymbol{u}}_h, \boldsymbol{u}_h, \boldsymbol{q}_h), \boldsymbol{w} \right\rangle_{\partial \mathcal{T}_h} = 0,
\tag{4b}
$$

$$
\left\langle \widehat{\boldsymbol{f}}_h(\widehat{\boldsymbol{u}}_h, \boldsymbol{u}_h, \boldsymbol{q}_h), \boldsymbol{\mu} \right\rangle_{\partial \mathcal{T}_h \backslash \partial \Omega} + \left\langle \widehat{\boldsymbol{b}}_h(\widehat{\boldsymbol{u}}_h, \boldsymbol{u}_h, \boldsymbol{q}_h), \boldsymbol{\mu} \right\rangle_{\partial \Omega} = 0,
\tag{4c}
$$

for all $(\boldsymbol{r}, \boldsymbol{w}, \boldsymbol{\mu}) \in \mathcal{Q}_h^k \times \mathcal{V}_h^k \times \mathcal{M}_h^k$ and all $t \in (0, T)$. The numerical flux $\widehat{\boldsymbol{f}}_h$ is defined as

$$
\widehat{\boldsymbol{f}}_h(\widehat{\boldsymbol{u}}_h, \boldsymbol{u}_h, \boldsymbol{q}_h; \boldsymbol{n}) = \boldsymbol{F}(\widehat{\boldsymbol{u}}_h, \boldsymbol{q}_h) \cdot \boldsymbol{n} + \boldsymbol{\sigma}(\widehat{\boldsymbol{u}}_h, \boldsymbol{u}_h; \boldsymbol{n}) \cdot (\boldsymbol{u}_h - \widehat{\boldsymbol{u}}_h),
\tag{5}
$$

where $\boldsymbol{\sigma}$ denotes the stabilization matrix. In this work, we set $\boldsymbol{\sigma} = \lambda_{max}(\widehat{\boldsymbol{u}}_h)$.[14] The semi-discrete system (4) is further discretized in time using L-stable, diagonally implicit Runge-Kutta (DIRK) schemes.[2] The interested reader is referred to[11–13] for a detailed description of the numerical discretization and the nomenclature above. We emphasize that the shock capturing method in this paper applies to other numerical schemes and working variables, such as primitive and entropy variables.

III.   Sensors

In this section, we present physics-based sensors to detect the unstable SGS features that may appear in the simulation of fluid flows, namely, shock waves and high-gradient features such as shear and thermal layers.

A.   Shock sensor

The goal of the shock sensor is to identify shock waves. As such, it is to activate in shocks and vanish elsewhere, including smooth regions of the flow and other unstable subgrid-scale features. To this end, we propose a shock sensor $\hat{s}_\beta$ of the form

$$\hat{s}_\beta(\boldsymbol{x}) = f\big(s_\beta;\ s_{\beta,thr}, s_{\beta,min}, s_{\beta,max}\big), \qquad\qquad s_\beta(\boldsymbol{x}) = s_d \cdot s_\omega, \qquad (6)$$

where s_d is a dilatation sensor and s_ω is a vorticity sensor. The dilatation sensor is to activate in shock waves. The vorticity sensor is to vanish in vorticity-dominated regions of the flow, in which $|\nabla \cdot \boldsymbol{v}| \ll |\nabla \times \boldsymbol{v}|$, as well as in non-shocky regions in which $(-\nabla \cdot \boldsymbol{v})$ is large due to under-resolution. In particular, the dilatation and vorticity[10] sensors read as follows

$$s_d(\boldsymbol{x}) = -\frac{h_\beta}{k}\frac{\nabla \cdot \boldsymbol{v}}{c^*}\ , \qquad\qquad s_\omega(\boldsymbol{x}) = \frac{(\nabla \cdot \boldsymbol{v})^2}{(\nabla \cdot \boldsymbol{v})^2 + |\nabla \times \boldsymbol{v}|^2 + \epsilon_\omega}, \qquad (7)$$

where

$$h_\beta(\boldsymbol{x}) = h_{ref}\ \frac{|\nabla\rho|}{\big(\nabla\rho^t \cdot \boldsymbol{M}_h^{-1} \cdot \nabla\rho + \epsilon_h\big)^{1/2}}, \qquad (8)$$

is the characteristic element size along the direction of the density gradient, k denotes the polynomial order of the numerical approximation, $c^* = c^*(\boldsymbol{x})$ is the speed of sound at the critical temperature $T^* = T^*(\boldsymbol{x})$, $|\cdot|$ denotes the Euclidean norm, $\boldsymbol{M}_h = \boldsymbol{M}_h(\boldsymbol{x})$ is the metric tensor of the mesh, h_{ref} the reference element size used in the construction of $\boldsymbol{M}_h$, and $\epsilon_\omega, \epsilon_h \sim \epsilon_m^2$ are constants of order machine epsilon squared. Also, dropping the subscript β to simplify notation,

$$f\big(s;\ s_{th}, s_{min}, s_{max}\big) = g(s) - \big(g(s) - s_{max}\big)\left[\frac{1}{\pi}\arctan\big(c_1\big(g(s) - s_{max}\big)\big) + \frac{1}{2}\right] - \frac{1}{\pi}\arctan(c_1) + \frac{1}{2}, \quad (9a)$$

$$g\big(s;\ s_{th}, s_{min}\big) = s_{min} + \big(s - s_{th} - s_{min}\big)\left[\frac{1}{\pi}\arctan\big(c_1\big(s - s_{th} - s_{min}\big)\big) + \frac{1}{2}\right] - \frac{1}{\pi}\arctan(c_1) + \frac{1}{2}, \quad (9b)$$

with $c_1 \gg 1$, are smooth surrogates for $\min\big\{g(s), s_{max}\big\}$ and $\max\{s - s_{th}, s_{min}\}$, respectively. We note that s_β is uniformly bounded above for stationary $\partial(\cdot)/\partial t = 0$, plane-parallel $\partial(\cdot)/\partial y = \partial(\cdot)/\partial z = 0$ shocks, namely,

$$\begin{aligned}
s_{\beta,max}^{th} &= \sup_{M_{1n}\geq 1} s_\beta \leq \sup_{M_{1n}\geq 1} s_d \approx \sup_{M_{1n}\geq 1} -\frac{h_\beta/k}{c^*}\frac{\Delta v_n}{\delta_s} \\
&\approx \sup_{M_{1n}\geq 1}\frac{h_\beta/k}{\delta_s}\frac{2M_{1n}^2 - 2}{(\gamma+1)M_{1n}}\sqrt{\frac{\gamma+1}{2+(\gamma-1)M_{1n}^2}} = \frac{h_\beta/k}{\delta_s}\frac{2}{\sqrt{\gamma^2-1}} \leq \frac{2}{\sqrt{\gamma^2-1}},
\end{aligned} \qquad (10)$$

where δ_s denotes the thickness of the shock in the numerical solution, and the superscript th stands for the theoretical upper limit of s_β. We take advantage of this property by setting $s_{\beta,max} = s_{\beta,max}^{th}$. Similarly, setting $s_{\beta,min} = 0$ ensures that no negative artificial viscosity is introduced in the scheme. Also, without these lower and upper bounds in the sensor, numerical oscillations could produce non-physical values of s_β that positively reinforce the oscillations and lead to the simulation breakdown. Finally, the threshold $s_{\beta,thr}$ is set to 0.01. This value typically suffices to avoid the introduction of artificial bulk viscosity in acoustic waves and vortical structures, while having a minor impact in shock waves.

American Institute of Aeronautics and Astronautics

B. Thermal sensor

The purpose of the thermal sensor $\hat{s}_\kappa$ is to detect thermal gradients that are larger than possible with the available resolution. These correspond to subgrid-scale features that may lead to nonlinear instability. In this spirit, we define

$$\hat{s}_\kappa(\boldsymbol{x}) = f\big(s_\kappa; s_{\kappa,thr}, s_{\kappa,min}, s_{\kappa,max}\big), \qquad s_\kappa(\boldsymbol{x}) = \frac{h_{ref}}{k} \frac{|\nabla_{\boldsymbol{\xi}} T|}{T_0}, \qquad (11)$$

where f is as in Eq. (9), $T_0 = T_0(\boldsymbol{x})$ denotes the stagnation temperature, and $\nabla_{\boldsymbol{\xi}} T$ is the temperature gradient under the metric of the reference element, that is,

$$\nabla_{\boldsymbol{\xi}} T = \frac{\partial T}{\partial \boldsymbol{\xi}_i} = \sum_{j \leq d} \frac{\partial T}{\partial \boldsymbol{x}_j} \frac{\partial \boldsymbol{x}_j}{\partial \boldsymbol{\xi}_i} = \boldsymbol{x}_{\boldsymbol{\xi}}^t \cdot \nabla_{\boldsymbol{x}} T, \qquad i = 1, \dots, d. \qquad (12)$$

Also, we set

$$s_{\kappa,thr} = 1 \approx s_{\kappa,max}^{th}, \qquad s_{\kappa,min} = 0, \qquad s_{\kappa,max} = 2 \approx 2\, s_{\kappa,max}^{th},$$

where $s_{\kappa,max}^{th} \approx 1$ is the maximum theoretical value of s_κ for temperature gradients that can be resolved with the available resolution. The definition of the thermal sensor above ensures that it is active only in regions with strong thermal gradients which are not resolved by the grid resolution. In particular, it can be shown that $s_\kappa \lesssim 4\gamma/(\gamma+1)^2 \leq 1 = s_{\kappa,thr}$ in stabilized stationary plane-parallel shock waves, regardless of the incident Mach number. Since shocks are stabilized by a mechanism that is independent of $\hat{s}_\kappa$, as described below, it is a desired property that the thermal sensor vanishes in shock waves.

C. Shear sensor

Finally, the shear sensor $\hat{s}_\mu$ reads as

$$\hat{s}_\mu(\boldsymbol{x}) = f\big(s_\mu; s_{\mu,thr}, s_{\mu,min}, s_{\mu,max}\big), \qquad s_\mu(\boldsymbol{x}) = \frac{h_{ref}}{k} \frac{||\mathcal{L}(\boldsymbol{v}) \cdot \boldsymbol{x}_{\boldsymbol{\xi}}^t||_2}{v_{max}}, \qquad (13)$$

where f is as in Eq. (9), $|| \cdot ||_2$ denotes the spectral norm,

$$\mathcal{L}(\boldsymbol{v}) = \nabla_{\boldsymbol{x}} \boldsymbol{v} - \text{diag}(\nabla_{\boldsymbol{x}} \boldsymbol{v}) = \frac{\partial \boldsymbol{v}_i}{\partial \boldsymbol{x}_j}\big(1 - \delta_{ij}\big),$$

and

$$v_{max}(\boldsymbol{x}) = \left(v^2 + \frac{2}{\gamma - 1} c^2\right)^{1/2}$$

is the maximum isentropic velocity, that is, the velocity of the fluid if all total energy was converted into kinetic energy through an isentropic expansion. The presence of the $\text{diag}(\nabla_{\boldsymbol{x}} \boldsymbol{v})$ term in $\mathcal{L}(\boldsymbol{v})$ is for the shear sensor to vanish in shock waves.

We emphasize that, like the thermal sensor, the purpose of the shear sensor is to detect velocity gradients that are larger than possible with the available resolution and could therefore lead to nonlinear instability and the simulation breakdown. In this spirit, we set

$$s_{\mu,thr} = 1 \approx s_{\mu,max}^{th}, \qquad s_{\mu,min} = 0, \qquad s_{\mu,max} = 2 \approx 2\, s_{\mu,max}^{th},$$

where $s_{\mu,max}^{th} \approx 1$ denotes the maximum theoretical value of s_μ for resolved scales. This improves nonlinear stability and ensures the shear sensor activates only for potentially unstable subgrid-scale features. In particular, $s_{\mu,thr} = 1$ ensures again the shear sensor vanishes in stabilized stationary plane-parallel shock waves, regardless of the shock strength.

IV. Stabilization through artificial viscosity

We increase selected transport coefficients to resolve unstable sugbrid-scale features over the smallest distance allowed by the discretization. The bulk viscosity, thermal conductivity and shear viscosity are thus given by the contribution of the physical $(\beta_f, \kappa_f, \mu_f)$ and artificial $(\beta^*, \kappa^*, \mu^*)$ values, that is,

$$\beta = \beta_f + \beta^*, \qquad \kappa = \kappa_f + \kappa^* = \kappa_f + \kappa_1^* + \kappa_2^*, \qquad \mu = \mu_f + \mu^*.$$

Shock waves, thermal gradients and shear gradients are stabilized by increasing the bulk viscosity, thermal conductivity and shear viscosity, respectively. (The thermal conductivity is also augmented in shock waves through the term κ_1^*, as discussed below.) This is consistent with mathematical and physical arguments that identify these as the mechanisms responsible for stabilizing, in the sense of avoiding finite-time singularities, these various flow features. Also, this is consistent with our choice of sensors as the penalty is imposed directly to the fields that are used for sensing.

We emphasize that shock waves are stabilized through β^* and κ_1^* only. The later term is used to obtain $\theta_s \approx \delta_s$ and improve nonlinear stability in hypersonic regimes, where θ_s denotes the thermal thickness of the shock. While artificial shear viscosity can also stabilize shock waves, the former approach is preferred here. First, it does not pollute the off-diagonal terms in the viscous stress tensor so that sharper shock profiles are obtained. Second and more importantly, it minimizes the dissipation of vortical structures crossing the shock.[27] The particular form of the artificial transport coefficients reads as follows:

$$\beta^* = \Phi_\beta \left[\rho \, \frac{k_\beta \, h_\beta(\boldsymbol{x})}{k} \left(v^2(\boldsymbol{x}) + c^{*2}(\boldsymbol{x}) \right)^{1/2} \hat{s}_\beta(\boldsymbol{x}) \right], \tag{14a}$$

$$\kappa^* = \kappa_1^* + \kappa_2^* = \frac{c_p}{Pr_\beta^*} \, \beta^* + \Phi_\kappa \left[\rho \, c_p \, \frac{k_\kappa \, h_\kappa(\boldsymbol{x})}{k} \left(v^2(\boldsymbol{x}) + c^{*2}(\boldsymbol{x}) \right)^{1/2} \hat{s}_\kappa(\boldsymbol{x}) \right], \tag{14b}$$

$$\mu^* = \Phi_\mu \left[\rho \, \frac{k_\mu \, h_\mu(\boldsymbol{x})}{k} \left(v^2(\boldsymbol{x}) + c^{*2}(\boldsymbol{x}) \right)^{1/2} \hat{s}_\mu(\boldsymbol{x}) \right], \tag{14c}$$

where $\Phi_{\{\beta,\kappa,\mu\}}[\,\cdot\,]$ are smoothing operators, Pr_β^* is an artificial Prandtl number, $k_{\{\beta,\kappa,\mu\}}$ are positive constants, and

$$h_\kappa(\boldsymbol{x}) = h_{ref} \, \frac{|\nabla_{\boldsymbol{x}} T|}{\left(\nabla_{\boldsymbol{x}} T^t \cdot \boldsymbol{M}_h^{-1} \cdot \nabla_{\boldsymbol{x}} T + \epsilon_h \right)^{1/2}}, \tag{15a}$$

$$h_\mu(\boldsymbol{x}) = h_{ref} \, \sigma_{min}(\boldsymbol{M}_h) = h_{ref} \, \inf_{|\boldsymbol{a}|=1} \left\{ \boldsymbol{a}^t \cdot \boldsymbol{M}_h \cdot \boldsymbol{a} \right\}, \tag{15b}$$

are the element size in the direction of the temperature gradient and the smallest element size among all possible directions, respectively. The theoretical values of k_β and Pr_β^* in order to optimally resolve a stationary plane-parallel shock over a thickness $\delta_s, \theta_s \approx h_\beta/k$ can be shown to be of order one. In particular, we set $k_{\{\beta,\kappa,\mu\}} = 1.5$ and $Pr_\beta^* = 0.9$ due to the sharp shock resolutions obtained with this choice for one-dimensional shocks.

Smoothing operators

Large inter-element jumps in the numerical solution, such as in under-resolved sharp features, lead to large discontinuouties in the artificial viscosity fields. This may degrade the accuracy of the solution and lead to numerical instabilities.[3,36] Hence, we equip the artificial transport coefficients with smoothing operators $\Phi_{\{\beta,\kappa,\mu\}}$ that map onto a $\mathcal{C}^\alpha$-continuous approximation space. In our experience, further smoothness beyond $\alpha = 0$ does not provide additional stability. This is consistent with the fact that the artificial transport coefficients only enter in the discrete system (4) through the terms $(\boldsymbol{F}, \nabla \boldsymbol{w})_{\mathcal{T}_h}$, $\langle \widehat{\boldsymbol{f}}_h, \boldsymbol{w} \rangle_{\partial \mathcal{T}_h}$, $\langle \widehat{\boldsymbol{f}}_h, \boldsymbol{\mu} \rangle_{\partial \mathcal{T}_h \setminus \partial \Omega}$ and $\langle \widehat{\boldsymbol{b}}_h, \boldsymbol{\mu} \rangle_{\partial \Omega}$. As such, the notion of $\mathcal{C}^\alpha$-continuity for $\alpha > 0$ is lost upon discretization.

Convolution with a truncated Gaussian filter,[9] projection onto a lower dimensional continuous approximation space, and elementwise reconstruction procedures[28] are examples of smoothing operators. The appropiate choice of smoothing operators depends on the numerical scheme and the accuracy order at hand. In this work, we employ an elementwise linear reconstruction procedure analogous to that introduced in[28] for the element size. A comparison of smoothing operators will be presented in future work. We shall omit further details here.

V. Numerical examples

We examine the performance of the method on several unsteady flows in transonic, supersonic and hypersonic regimes. Two-dimensional and three-dimensional problems, as well as different accuracy orders, are considered. All results are presented in non-dimensional form.

A. Inviscid strong-vortex/shock-wave interaction

Case description and numerical discretization

We consider the two-dimensional inviscid interaction between a strong vortex and a shock wave. The problem domain is $\Omega = (0, 2L) \times (0, L)$ and a stationary normal shock wave is located at $x_s = L/2$. A counter-clockwise rotating vortex is initially located upstream of the shock and advected downstream by the inflow velocity. In particular, the inflow Mach number is $M_\infty = 1.5$ and the vortex is initially radius $b = 0.175\,L$ and centered at $(x, y) = (L/4,\ L/2)$. The initial velocity, temperature, density and pressure fields upstream the shock are given by

$$\boldsymbol{v}(r) = \boldsymbol{v}_\theta(r) + u_\infty\,\hat{\boldsymbol{e}}_x, \qquad \boldsymbol{v}_\theta(r) = u_m\,\hat{\boldsymbol{e}}_\theta \cdot \begin{cases} \frac{r}{a} & \text{if } r \leq a, \\ \frac{a}{a^2 - b^2}\left(r - \frac{b^2}{r}\right) & \text{if } a \leq r \leq b, \\ 0 & \text{if } b \leq r, \end{cases} \tag{16a}$$

$$T(r) = \begin{cases} T_\infty - \int_r^b \frac{1}{c_p} \frac{|\boldsymbol{v}_\theta(r')|^2}{r'}\,dr' & \text{if } r < b, \\ T_\infty & \text{if } b \leq r, \end{cases}, \qquad \rho(r) = \rho_\infty\left(\frac{T(r)}{T_\infty}\right)^{\frac{1}{\gamma-1}}, \qquad p(r) = p_\infty\left(\frac{T(r)}{T_\infty}\right)^{\frac{\gamma}{\gamma-1}}, \tag{16b}$$

where $a = 0.075\,L$ is a constant, r denotes the distance to the vortex center, $u_m = 3\,u_\infty\,/\,5$ is the maximum tangential velocity of the vortex, u_∞ the inflow velocity magnitude, T_∞ the inflow temperature, and $\hat{\boldsymbol{e}}_x$ and $\hat{\boldsymbol{e}}_\theta$ are unit vectors along the x- and the tangential (around the vortex center) directions, respectively. The initial condition downstream the shock wave is obtained from one-dimensional stationary shock wave theory.

The computational domain is partitioned using 400×200 uniform quadrilateral elements, and the time-step size is set to $\Delta t = 3.00 \cdot 10^{-4}\,L\,u_\infty^{-1}$. Sixth-order IEDG[11] and third-order DIRK schemes are used for the spatial and temporal discretization, respectively. Slip wall boundary conditions are imposed on the top and bottom surfaces, whereas the characteristics-based, non-reflecting boundary condition in[13] is used on the inflow and outflow.
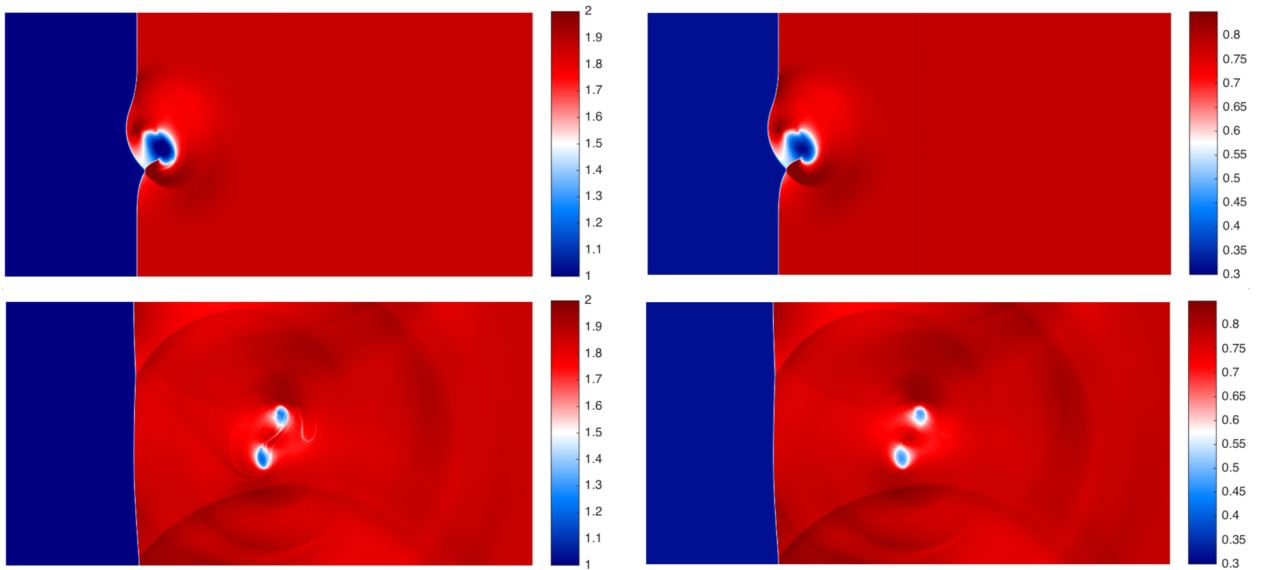

Figure 1: Non-dimensional density ρ/ρ_∞ (left) and pressure $p/(\rho_\infty u_\infty^2)$ (right) fields of the strong-vortex/shock-wave interaction problem at the target times t_1 (top) and t_2 (bottom). After the shock wave and the vortex meet, strong acoustic waves are generated and propagate on the downstream side of the shock.

Numerical results

Figure 1 shows the density and pressure fields at the target times $t_1 = 0.35 \, \gamma^{1/2} L \, u_\infty^{-1}$ and $t_2 = 1.05 \, \gamma^{1/2} L \, u_\infty^{-1}$. When the shock wave and the vortex meet, the former is distorted and the later split into two separate vortical structures. Strong acoustic waves are then generated from the moving vortex and propagate on the downstream side of the shock. The Mach number fields, together with zooms around the shock wave and the details of the computational mesh, are shown in Figure 2. The shock is non-oscillatory and resolved within one element.

The artificial bulk viscosity β^*, artificial thermal conductivity κ_2^* and artificial shear viscosity μ^* fields at the target times are shown in Figure 3. Despite the strong pressure waves and the correspondingly large negative velocity divergence at t_2, the shock sensor $\hat{s}_\beta$ vanishes everywhere outside the shock wave. Similarly, it is active only in the shock wave at t_1 despite the strong interaction between the vortex and the shock at this time. This is indeed the case for all time steps the simulation was performed. We note that, while κ_2^* and μ^* vanish in the entire domain, these stabilization mechanisms are required for more complex flows as illustrated with the hypersonic and turbomachinery flows considered next.

B.   Two-dimensional hypersonic cylinder

Case description and numerical discretization

We consider the hypersonic flow around a two-dimensional adiabatic cylinder at Reynolds number $Re_\infty = \rho_\infty u_\infty d/\mu = 376,930$ and Mach number $M_\infty = u_\infty/c_\infty = 17.605$, where ρ_∞, u_∞, c_∞, and d denote the freestream density, freestream velocity, freestream speed of sound, and cylinder diameter, respectively. The computational domain spans 2.5 diameters away from the center of the cylinder and is discretized using an isoparametric O-mesh with 16,000 quadrilateral elements. The time-step size is set to $\Delta t = 10^{-3} \, d/u_\infty$. Forth-order HDG and third-order DIRK schemes are used in this example.

Numerical results

Figure 4 shows the time-averaged pressure (left) and skin friction (right) coefficients on the upstream half of the cylinder. Snapshots of the temperature, velocity magnitude and vorticity fields are shown in Figure 5. A zoom of the Mach number field around the center of the shock, together with the details of the computational mesh, are shown in
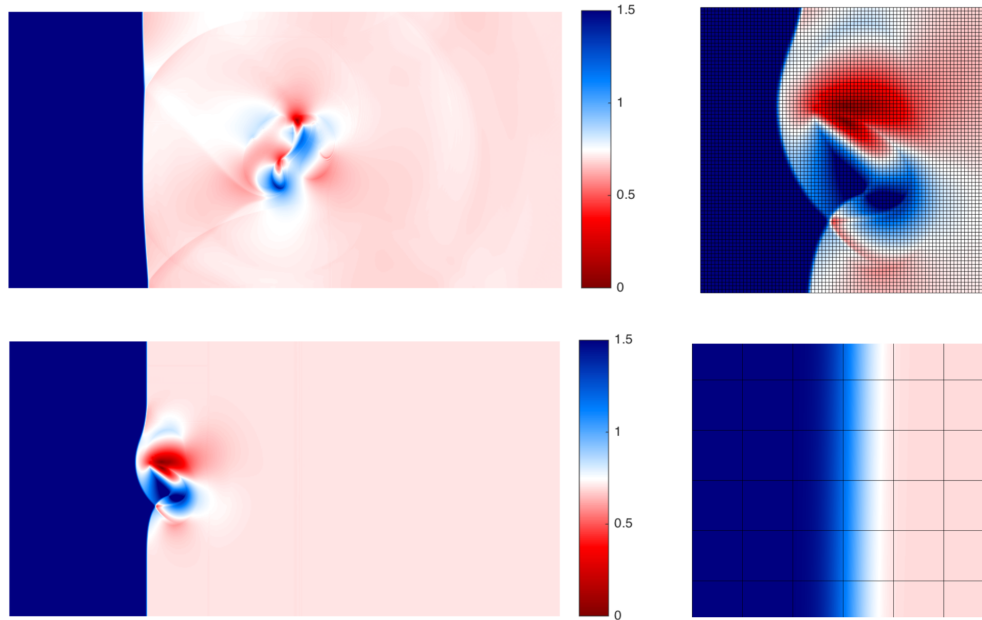

Figure 2: Mach number field of the strong-vortex/shock-wave interaction problem at the target times t_1 (top) and t_2 (bottom). Zooms around the shock wave are shown on the right images. The shock is non-oscillatory and resolved within one element.
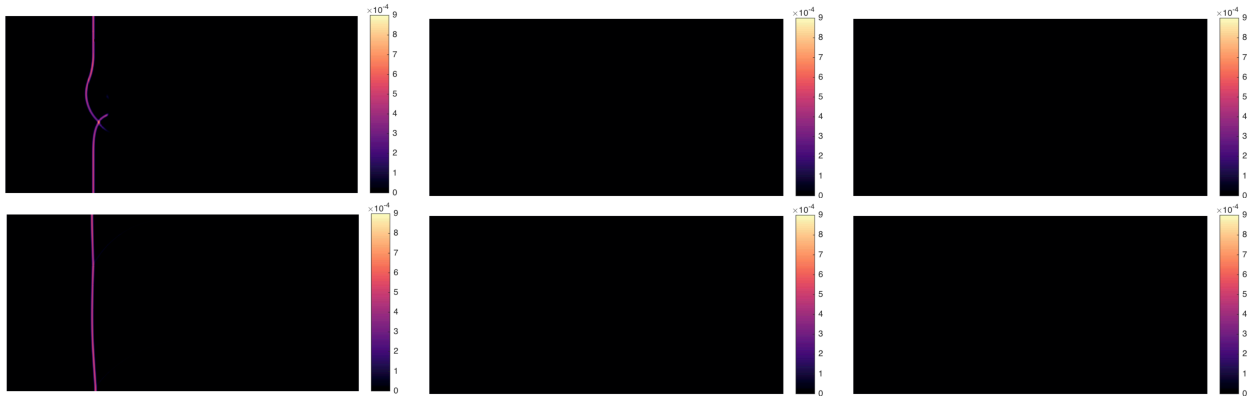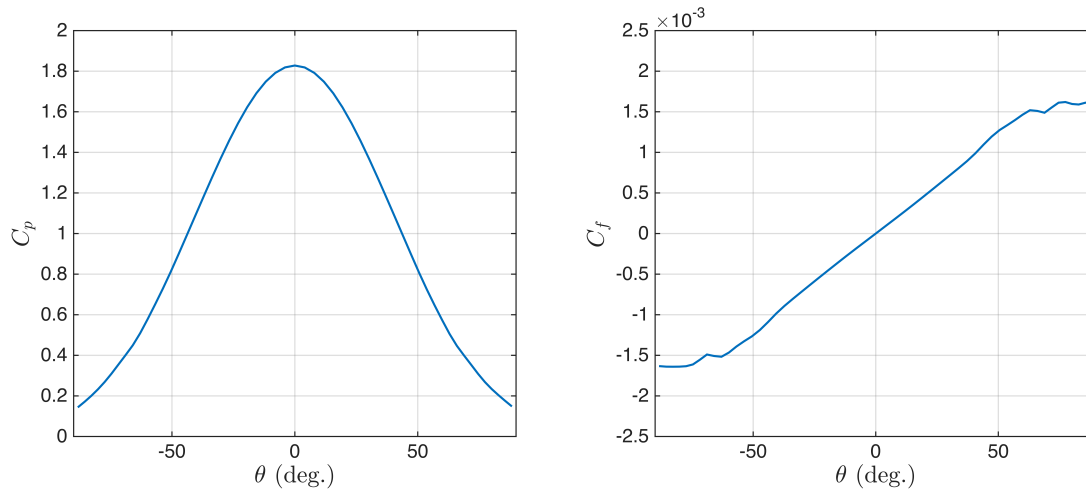
Figure 3: Snapshot of the non-dimensional artificial bulk viscosity $\beta^* \rho_\infty^{-1} u_\infty^{-1} L^{-1}$ (left), artificial thermal conductivity $\kappa_2^* \gamma \rho_\infty^{-1} u_\infty^{-1} c_p^{-1} L^{-1}$ (center) and artificial shear viscosity $\mu^* \rho_\infty^{-1} u_\infty^{-1} L^{-1}$ (right) fields of the strong-vortex/shock-wave interaction problem at the target times t_1 (top) and t_2 (bottom). Note β^* vanishes outside the shock, including the strong vortex and acoustic waves.

Figure 4: Time-averaged pressure (left) and skin friction (right) coefficients on the upstream half of the hypersonic cylinder.

the bottom right of this figure. Despite the high incident Mach number $M_1 = 17.6$, the shock is non-oscillatory and resolved within three elements.

Figure 6 shows a snapshot of the artificial thermal conductivity κ_2^* and artificial shear viscosity μ^* fields. Both the thermal and shear sensors vanish in the shock wave. Unlike in the strong-vortex/shock-wave interaction problem, the artificial thermal conductivity is non-zero in some small region downstream the cylinder. This corresponds to an unstable subgrid-scale thermal feature that cannot be stabilized with a *shock capturing only* approach. Indeed, removing κ_2^* from the model leaded to the simulation breakdown. The addition of κ_2^* stabilizes this feature while not affecting the shock wave. This exemplifies the need to stabilize other under-resolved sharp features than shock waves for the simulation of high Reynolds, high Mach number unsteady flows.

C. Transonic T106C low-pressure turbine

Case description and numerical discretization

Finally, we consider the three-dimensional transonic flow around the T106C linear low-pressure turbine (LPT) in off-design conditions. The isentropic Reynolds and Mach numbers on the outflow are $Re_{2,s} = 100,817$ and $M_{2,s} = 0.987$, respectively, whereas the angle between the inflow velocity and the longitudinal direction is $\alpha_1 = 50.54$ deg.
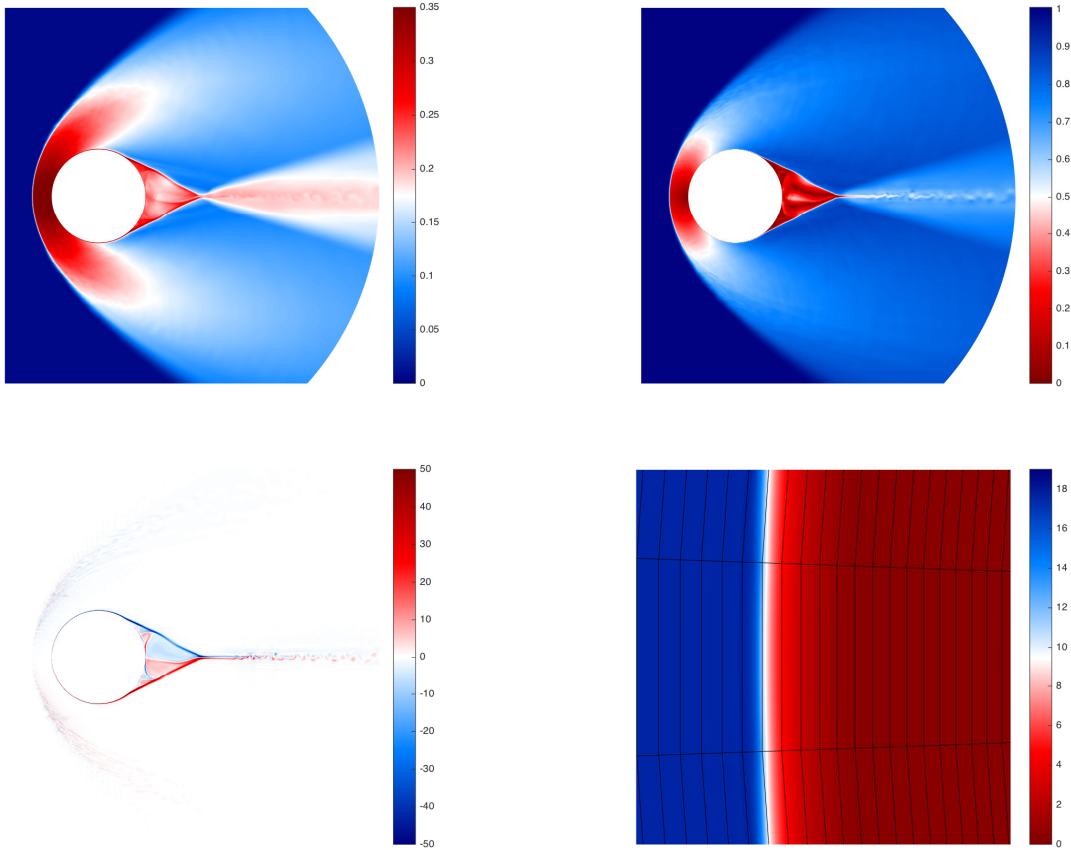
Figure 5: Snapshot of the non-dimensional temperature $c_p\,T/\gamma\,u_\infty^2$ (top left), velocity magnitude $|\boldsymbol{v}|/u_\infty$ (top right) and vorticity $d\,(\nabla \times \boldsymbol{v})/u_\infty$ (bottom left) fields for the hypersonic cylinder. A zoom of the Mach number field around the center of the shock is shown in the bottom right image. Despite the high incident Mach number $M_1 = 17.6$, the shock is non-oscillatory and resolved within three elements.
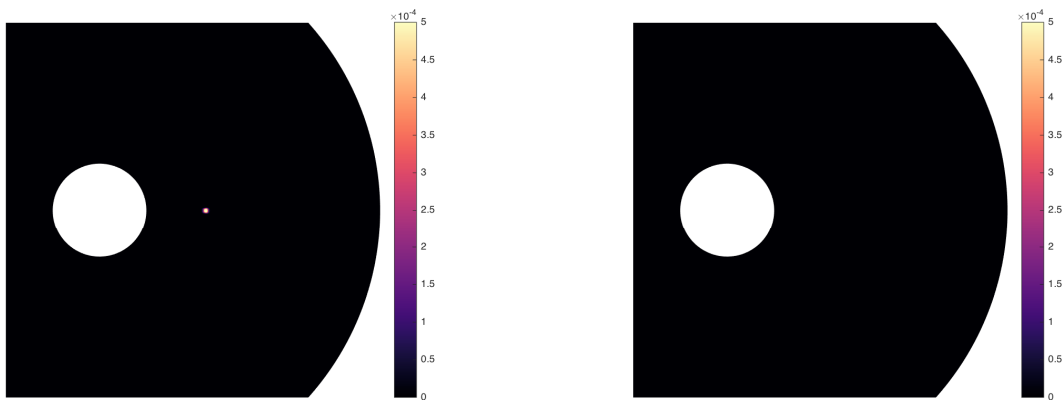

Figure 6: Snapshot of the non-dimensional artificial thermal conductivity $\kappa_2^*\,\gamma\,\rho_\infty^{-1}u_\infty^{-1}c_p^{-1}d^{-1}$ (left) and artificial shear viscosity $\mu^*\rho_\infty^{-1}u_\infty^{-1}d^{-1}$ (right) fields for the hypersonic cylinder. Note κ_2^* is non-zero in a small region downstream the cylinder. This corresponds to an unstable subgrid-scale thermal feature that cannot be stabilized with a *shock capturing only* approach.
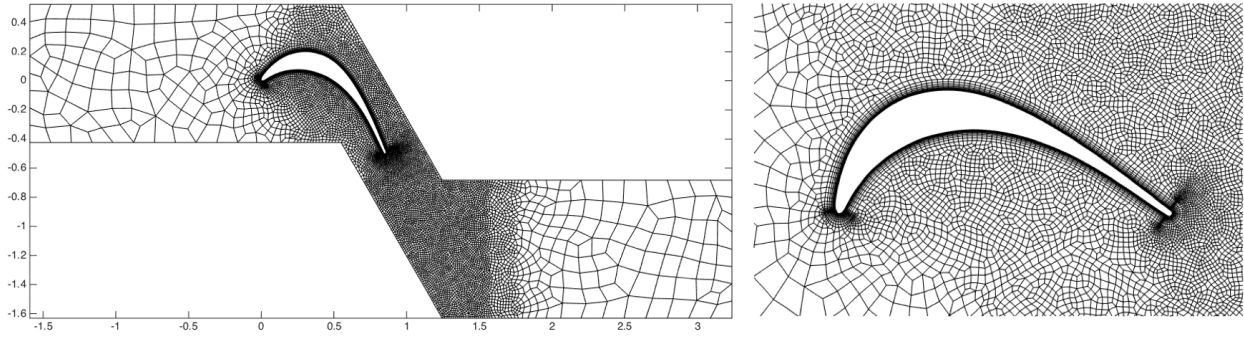
Figure 7: 2D slice of the computational mesh for the T106C low-pressure turbine. The tetrahedral mesh is created by subdividing each hexahedron into 6 tetrahedra.

The extrusion length in the spanwise direction is $0.1\,c_b$, where c_b denotes the blade chord. The computational mesh consists of 712,080 isoparametric tetrahedral elements and the time-step size is $\Delta t = 6.94 \cdot 10^{-3}\,c_b\,\sqrt{\rho_{1,0}/p_{1,0}}$, where $p_{1,0}$ and $\rho_{1,0}$ are the stagnation pressure and stagnation density at inlet, respectively. Third-order HDG and DIRK schemes are used for the discretization. A no-slip, adiabatic wall boundary condition is imposed on the blade surface, and a characteristics-based, non-reflecting boundary condition[13] is used on inflow and outflow. Periodicity is imposed on the tangential and spanwise directions. A 2D slice of the mesh is shown in Figure 7.[16]

Numerical results

Figure 8 shows the time- and spanwise-averaged isentropic Mach number (left) and skin friction coefficient (right) on the blade surface. The stagnation pressure at inlet $p_{1,0}$ is used for non-dimensionalization of the skin friction coefficient. The time-averaged (left) and instantaneous (right) pressure, temperature and Mach number fields are shown in Figure 9. Several unsteady shocks that oscillate around a baseline position are present in this flow, as illustrated by the smoother shock profiles in the average fields compared to the instantaneous fields. These unsteady shocks are resolved within one element. Also, from the spanwise vorticity fields in Figure 10, the shock capturing method seems to have little to no impact on the resolved vortical structures across the shock. This is justified by the minor role of the bulk viscosity on the vorticity equation. Further investigation on this topic is the subject of current work. Finally, we emphasize that both κ_2^* and μ^* were necessary to stabilize under-resolved thermal and shear features in this flow.
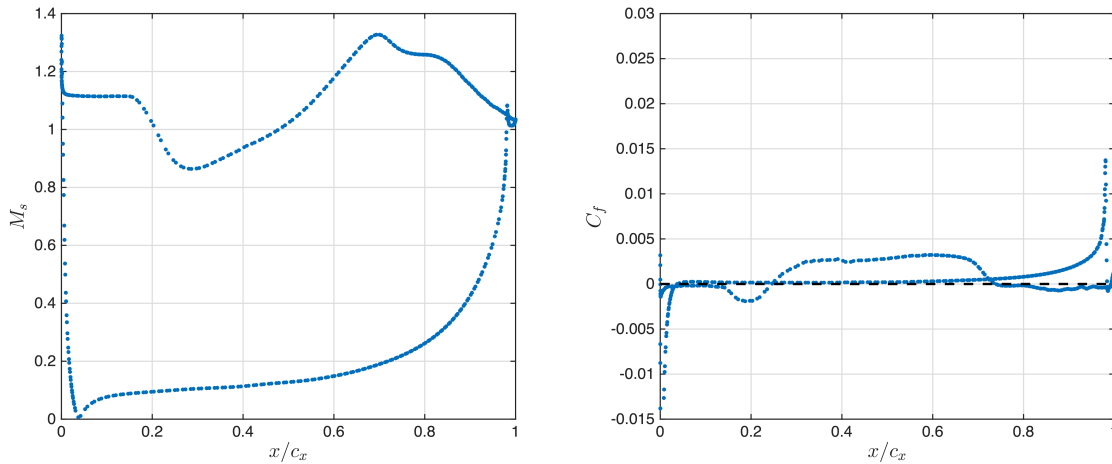

Figure 8: Isentropic Mach number M_s (left) and skin friction coefficient C_f (right) on the blade surface of the T106C LPT. The stagnation pressure at inlet is used for non-dimensionalization of the skin friction coefficient.

VI.   Conclusions

We presented a shock capturing method for unsteady laminar and turbulent flows. The proposed method performed robustly and provided non-oscillatory, sharp shock profiles for the transonic, supersonic, and hypersonic unsteady flows considered. We emphasize the need to stabilize other under-resolved sharp features than shock waves, including strong thermal and shear gradients, for the simulation of complex unsteady flows. Finally, while numerical results suggest the model has little to no impact on the resolved turbulent structures and acoustic waves, further investigation on this topic is the subject of ongoing research.
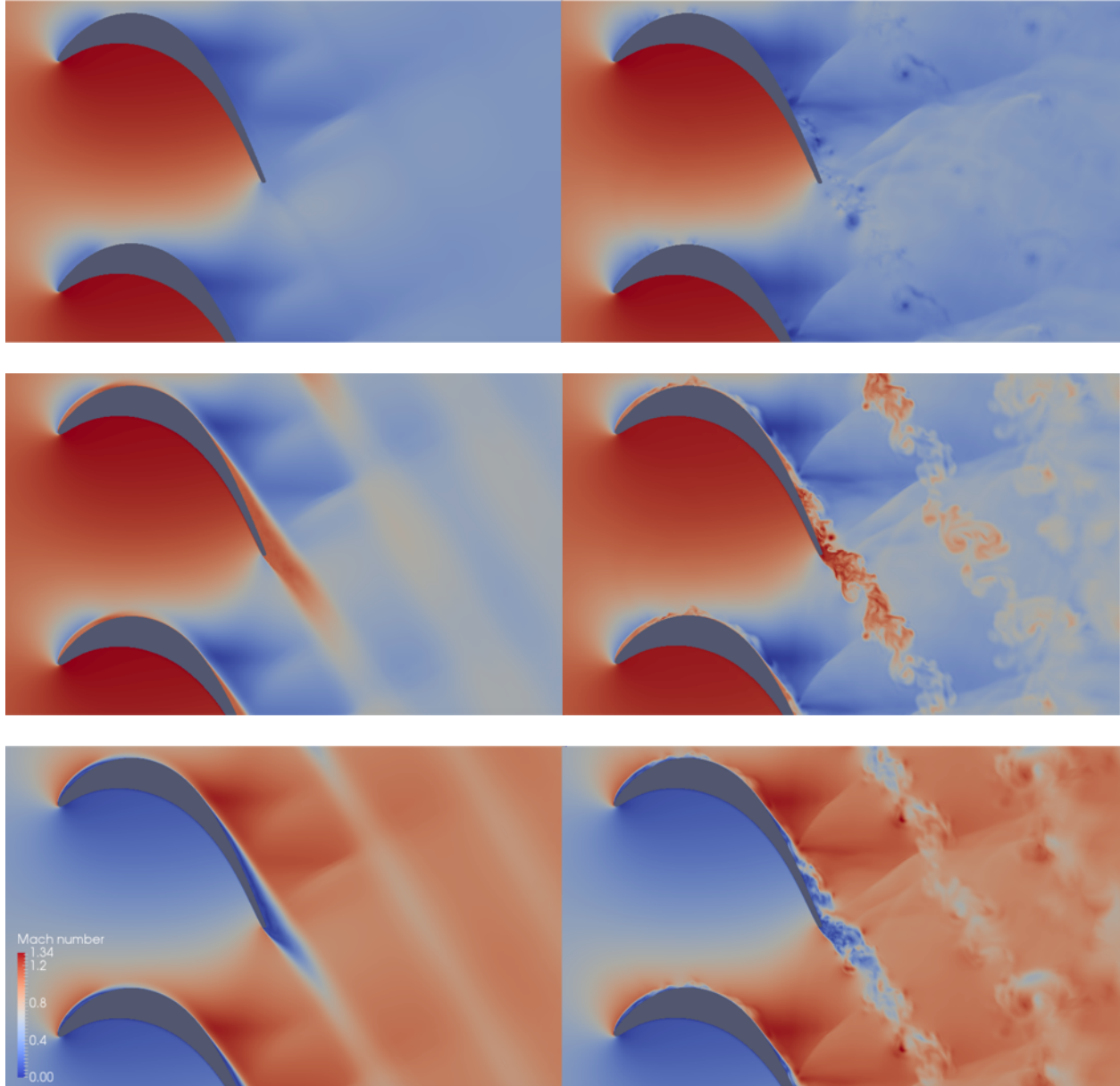

Figure 9: Pressure (top), temperature (center) and Mach number (bottom) fields for the transonic T106C LPT. Time-averaged and instantaneous fields are shown on the left and right images, respectively. The unsteady shocks involved are resolved within one element.

Figure 10: Time-averaged (left) and instantaneous (right) spanwise vorticity fields for the transonic T106C LPT. The shock capturing method seems to have little to no impact on the resolved vortical structures across the shock.

Acknowledgments

References

[1] H. Abbassi, F. Mashayek, G.B. Jacobs, Shock capturing with entropy-based artificial viscosity for staggered grid discontinuous spectral element method, Comput. Fluids 98 (2014) 152–163.

[2] R. Alexander, Diagonally implicit Runge-Kutta methods for stiff ODEs, SIAM J. Numer. Anal. 14 (6) (1977) 1006–1021.

[3] G.E. Barter, D.L. Darmofal, Shock capturing with PDE-based artificial viscosity for DGFEM: Part I. Formulation, J. Comput. Phys. 229 (5) (2010) 1810–1827.

[4] A. Burbeau, P. Sagaut, C.H. Bruneau, A problem-independent limiter for high order Runge-Kutta discontinuous Galerkin methods, J. Comput. Phys. 169 (2001) 111–150.

[5] B. Cockburn, C.-W. Shu, TVB Runge-Kutta local projection discontinuous Galerkin methods for scalar conservation laws II: General framework, Math. Comp. 52 (1989) 411–435.

[6] B. Cockburn, C.W. Shu, The Runge-Kutta discontinuous Galerkin method for conservation laws V: multidimensional systems, J. Comput. Phys. 141 (1998) 199–224.

[7] B. Cockburn, J. Gopalakrishnan, R. Lazarov, Unified hybridization of discontinuous Galerkin, mixed and continuous Galerkin methods for second order elliptic problems, SIAM J. Numer. Anal. 47 (2) (2009) 1319–1365.

[8] B. Cockburn, J. Guzman, S.C. Soon, H.K. Stolarski, An Analysis of the Embedded Discontinuous Galerkin Method for Second-Order Elliptic Problems, SIAM J. Numer. Anal. 47 (4) (2009) 2686–2707.

[9] A.W. Cook, W.H. Cabot, Hyperviscosity for shock-turbulence interactions, J. Comput. Phys. 203 (2005) 379–385.

[10] F. Ducros, V. Ferrand, F. Nicoud, C. Weber, D. Darracq, C. Gacherieu, T. Poinsot, Large-Eddy Simulation of the Shock/Turbulence Interaction, J. Comput. Phys. 152 (1999) 517–549.

[11] P. Fernandez, N.C. Nguyen, X. Roca, J. Peraire, Implicit large-eddy simulation of compressible flows using the Interior Embedded Discontinuous Galerkin method, In: 54th AIAA Aerospace Sciences Meeting, San Diego, USA, 2016.

[12] P. Fernandez, High-Order Implicit-Large Eddy Simulation for Transitional Aerodynamic Flows, Master Thesis, Department of Aeronautics and Astronautics, Massachusetts Institute of Technology, 2016.

[13] P. Fernandez, N.C. Nguyen, J. Peraire, The hybridized Discontinuous Galerkin method for Implicit Large-Eddy Simulation of transitional turbulent flows, J. Comput. Phys. 336 (1) (2017) 308–329.

[14] P. Fernandez, N.C. Nguyen, J. Peraire, Subgrid-scale modeling and implicit numerical dissipation in DG-based Large-Eddy Simulation, In: 23rd AIAA Computational Fluid Dynamics Conference, Denver, USA, 2017.

[15] R. Hartmann, Higher-order and adaptive discontinuous Galerkin methods with shock-capturing applied to transonic turbulent delta wing flow, Int. J. Numer. Meth. Fluids 72 (2013) 883–894.

[16] K. Hillewaert, C. Carton de Wiart, G. Verheylewegen, T. Arts, Assessment of a High-Order Discontinuous Galerkin Method for the Direct Numerical Simulation of Transition at Low-Reynolds Number in the T106C High-Lift Low Pressure Turbine Cascade, In: ASME Turbo Expo 2014: Turbine Technical Conference and Exposition, Dusseldorf, Germany, 2014.

[17] K. Hillewaert, J.S. Cagnone, S.M. Murman, A. Garai, Y. Lv, M. Ihme, Assessment of high-order DG methods for LES of compressible flows, In: Proceedings of the Center for Turbulence Research Summer Program 2016.

[18] E. Johnsen, J. Larsson, A.V. Bhagatwala, *et al.*, Assessment of high-resolution methods for numerical simulations of compressible turbulence with shock waves, J. Comput. Phys. 229 (2010) 1213–1237.

[19] S. Kawai, S.K. Lele, Localized artificial diffusivity scheme for discontinuity capturing on curvilinear meshes, J. Comput. Phys. 227 (2008) 9498–9526.

[20] S. Kawai, K.S. Shankar, S.K. Lele, Assessment of localized artificial diffusivity scheme for large-eddy simulation of compressible turbulent flows, J. Comput. Phys. 229 (2010) 1739–1762.

[21] A. Klockner, T. Warburton, J.S. Hesthaven, Viscous shock-capturing in a time-explicit discontinuous Galerkin method, Math. Model. Nat. Phenom. 6 (2011) 57–83.

[22] L. Krivodonova, J. Xin, J.-F. Ramacle, N. Chevaugeon, J. E. Flaherty, Shock detection and limiting with Discontinuous Galerkin methods for hyperbolic conservation laws, Appl. Numer. Math. 48 (2004) 323–338.

[23] L. Krivodonova, Limiters for high order discontinuous Galerkin methods, J. Comput. Phys. 226 (2007) 879–896.

[24] H. Luo, J.D. Baum, R. Lohner, A Hermite WENO-based limiter for discontinuous Galerkin method on unstructured grids, J. Comput. Phys. 225 (2007) 686–713.

[25] Y. Lv, M. Ihme, Entropy-bounded discontinuous Galerkin scheme for Euler equations, J. Comput. Phys. 295 (2015) 715–739.

[26] Y. Lv, Y.C. See, M. Ihme, An entropy-residual shock detector for solving conservation laws using high-order discontinuous Galerkin methods, J. Comput. Phys. 332 (2016) 448–472.

[27] A. Mani, J. Larsson, P. Moin, Suitability of artificial bulk viscosity for large-eddy simulation of turbulent flows with shocks, J. Comput. Phys. 228 (2009) 7368–7374.

[28] D. Moro, N.C. Nguyen, J. Peraire, Dilation-based shock capturing for high-order methods, Int. J. Numer. Meth. Fluids 82 (2016) 398–416.

[29] N.C. Nguyen, J. Peraire, An Adaptive Shock-Capturing HDG Method for Compressible Flows, In: 20th AIAA Computational Fluid Dynamics Conference, Honolulu, USA, 2011.

[30] N.C. Nguyen, J. Peraire, Hybridizable discontinuous Galerkin methods for partial differential equations in continuum mechanics, J. Comput. Phys. 231 (18) (2012) 5955–5988.

[31] N.C. Nguyen, J. Peraire, B. Cockburn, A class of embedded discontinuous Galerkin methods for computational fluid dynamics, J. Comput. Phys. 302 (1) (2015) 674–692.

[32] B.J. Olson, S.K. Lele, Directional artificial fluid properties for compressible large-eddy simulation, J. Comput. Phys. 246 (2013) 207–220.

[33] J. Peraire, N.C. Nguyen, B. Cockburn, A Hybridizable Discontinuous Galerkin Method for the Compressible Euler and Navier-Stokes Equations, In: 48th AIAA Aerospace Sciences Meeting Including the New Horizons Forum and Aerospace Exposition, Orlando, USA, 2010.

[34] J. Peraire, N.C. Nguyen, B. Cockburn, An Embedded Discontinuous Galerkin Method for the Compressible Euler and Navier-Stokes Equations, In: 20th AIAA Computational Fluid Dynamics Conference, Honolulu, USA, 2011.

[35] P.-O. Persson, J. Peraire, Sub-Cell Shock Capturing for Discontinuous Galerkin Methods, In: 44th AIAA Aerospace Sciences Meeting and Exhibit, Reno, USA, 2006.

[36] P.-O. Persson, Shock capturing for high-order discontinuous Galerkin simulation of transient flow problems, In: 21th AIAA Computational Fluid Dynamics Conference, San Diego, USA, 2013.

[37] J.X. Qiu, C.W. Shu, Hermite WENO schemes and their application as limiters for Runge-Kutta discontinuous Galerkin method II: two dimensional case, Comput. Fluids 34 (2005) 642–663.

[38] J.V. Shebalin, Pseudospectral simulation of compressible turbulence using logarithmic variables, In: 11th AIAA Computational Fluid Dynamics Conference, Orlando, USA, 1993.

[39] J. Slotnick, A. Khodadoust, J. Alonso, D. Darmofal, W. Gropp, E. Lurie, D. Mavriplis, CFD Vision 2030 Study: A Path to Revolutionary Computational Aerosciences, NASA/CR-2014-218178, 2014.

[40] M. Sonntag, C-D. Munz, Efficient Parallelization of a Shock Capturing for Discontinuous Galerkin Methods using Finite Volume Sub-cells, J. Sci. Comput. 70 (3) (2017) 1262–1289.

[41] J. Yu, C. Yan, Z. Jiang, Revisit of dilation-based shock capturing for discontinuous Galerkin methods, Appl. Math. Mech. Engl. Ed., To Appear.

[42] J. Zhu, J. Qiu, C.W. Shu, M. Dumbser, Runge-Kutta discontinuous Galerkin method using WENO limiters II: unstructured meshes, J. Comput. Phys. 227 (2008) 4330–4353.